ELSEVIER

Engineering Sn doping Ni/chitosan to boost higher alcohols synthesis from direct coupling of aqueous ethanol: Modifying adsorption of aldehyde intermediates for C-C bond cleavage suppressing

Bo Chen [a], Xinqi Zheng [a], Juwen Gu [a], Songbai Qiu [a,b,c], Jinliang Song [a,b,c], Xiaoping Wu [a,b,c], Huafeng Dong [d], Qian Zhang [a,b,c,*], Tiejun Wang [a,b,c,*]

[a] *School of Chemical Engineering and Light Industry, Guangdong University of Technology, Guangzhou 510006, China*
[b] *Guangdong Provincial Key Laboratory of Plant Resources Biorefinery, Guangzhou 510006, China*
[c] *Guangzhou Key Laboratory of Clean Transportation Energy and Chemistry, Guangzhou 510006, China*
[d] *School of Physics and Optoelectronic Engineering, Guangdong University of Technology, Guangzhou 510006, China*

ABSTRACT

The direct aqueous ethanol coupling to higher alcohols is an essential bridge between abundant bio-ethanol and the outstanding application of higher alcohols as alternative jet-fuel or plasticizer precursors. In this work, the Sn-Ni/CS catalysts were developed, and the synergy between Ni and doped Sn species promoted the selective upgrading of ethanol to higher alcohols. Experimental and theoretical evidence revealed that the enhanced selectivity of higher alcohols was attributed to the weakened adsorption of midbody aldehydes over the catalyst and the suppression of the gas by-products, which was due to the change of the electron density around the Ni active site by Sn doping causing a rich electron set around Ni specie. Benefiting from the Sn doping, the Sn-Ni/CS-500–1/1 catalyst achieved > 85% selectivity for higher alcohols with 60% ethanol conversion at 230 °C.

1. Introduction

The problems of energy consumption and environmental destruction are getting worse, the biofuels and chemicals produced using renewable biomass are regarded as promising alternatives and additives to conventional petrochemical products such as diesel, jet-fuel and plasticizer [1–3]. Bioalcohols could be deemed as the most economically viable fuel additives because they have great potential for reduction of greenhouse gas and poisonous gas emissions as well as enhancement of energy efficiency, in which bio-ethanol from fermentation of sugar-containing biomass is the most productive liquid biofuel [4,5]. However, ethanol is hygroscopic, corrosive, and has low cetane number, which limits that ethanol is used as a blend additive for diesel at high proportions [4,6]. This problem related to ethanol can be mitigated by using C4 + alcohols [7]. Butanol and other higher alcohols can be blended with diesel at a higher rate than ethanol in internal combustion engines and is recognized as a good additives for diesel [8]. Besides, C8 + alcohols can be directly used to produce heterogeneous hydrocarbons with desired carbon chain lengths and properties of aviation fuel by one-step hydro-deoxygenation treatment, which is a potential alternative to

aviation fuel synthesis path [9,10]. In addition, C4 + alcohols have also been commonly used as plasticizers by esterification reaction to form various functional plasticizer products [11,12], which can be widely applied in food, medical, special cable and so on.

Although higher alcohols are promising alternative biofuels and plasticizer precursors, the large-scale production of higher alcohols from bio-feedstock remains challenging. The method reported recently is ABE (acetone-butanol-ethanol) fermentation process, which produces a mixture of acetone, butanol and ethanol at a low conversion rate [13]. However, considering the mature bio-ethanol industry, the direct upgrading of aqueous bio-ethanol into alternative higher alcohols has great attraction [14,15].

As a rule, the ethanol coupling to higher alcohols involves multi-step reactions: Ethanol is firstly dehydrogenated to acetaldehyde, and then to acetaldol via the aldol condensation. Followed by the dehydration and hydrogenation reactions, C4 + higher alcohols can form eventually [16, 17].

At present, various catalysts have been developed for ethanol upgrading reactions. The representative catalysts were listed in Table S1 to visualize the research progress of ethanol upgrading. As shown in

Table S1, for homogeneous catalysts such as Ir and Ru catalysts, high selectivity can be achieved, but it is difficult to separate the catalyst after reaction [18–20]. For heterogeneous catalysts like hydrotalcite, hydroxyapatite and so on, anhydrous ethanol feedstock is needed to prevent catalyst deactivation and the conversion is still low at the high reaction temperature [1,12,21,22]. Nevertheless, bioethanol produced by fermentation contains large amounts of water and the complexity as well as the cost of the refinement process leads to its extensive applications still a major techno-economic challenge. It will be much convenient/costless to directly upgrade aqueous ethanol into higher alcohols, even aqueous ethanol with concentration of 50 wt% can provide significant benefits in this regard. Therefore, it is essential that a highly water-resistant catalyst is developed for the C-C coupling of aqueous ethanol into higher alcohols.

Many transition metals usually exhibit strong dehydrogenation or hydrogenation capacity including Cu, Ni, etc. [23]. Especially, nickel has better hydrogenation or dehydrogenation capacity than Cu. However, the adsorption of hydrogen on Ni is too strong, which can result in deep dehydrogenation of ethanol to form gas by-products. Alloying the nickel can weaken the hydrogen binding energy, which can make the adsorption and desorption of hydrogen atoms achieve a balance [24]. Compared to nickel, the tin has weaker hydrogen binding, which is considered as an ideal substitute [25]. Therefore, the Sn-Ni alloy catalyst may prevent ethanol from deep dehydrogenation to enhance the C-C coupling reaction [26,27].

Porous carbon structure with electron-transporting and hydrophobicity is a promising matrix to disperse nanoparticles, which can effectively overcome the aggregation problem and enhance the stability of catalyst in aqueous environment [28,29]. Chitosan (CS) is produced by chitin derived from the shells of crustacean, which is the world's second hugest amount of naturally occurring polysaccharide [30,31]. Chitosan with hydroxyl, amino and carboxyl groups is a biopolymer, which has a strong affinity to transition metals. Therefore, chitosan is widely applied as a support of catalysts [25,32].

Herein, we fabricated a Sn-Ni/CS nanocomposite to boost higher alcohols synthesis by direct coupling of aqueous ethanol. The chitosan not only served as a reducing agent but also prevented the accumulation of the metal nanoparticles in the aqueous reaction system. This work investigated the performance of the Sn-Ni/CS catalyst with different preparation conditions for upgrading of aqueous ethanol. Furthermore, we investigated the Sn-Ni/CS catalysts on its structural and electronic properties by doping Sn. Combing experimental studies, catalyst characterizations and DFT calculations, the enhancement mechanism of higher alcohols selectivity by doping Sn was revealed.

2. Experimental section

2.1. Catalyst synthesis

The Sn-Ni/CS catalysts were synthesized by facile sol-gel technology [25,33]. Chitosan, $Ni(NO_3)_2 \cdot 6H_2O$ and $SnCl_4 \cdot 5H_2O$ were obtained from Macklin Biochemical Co., Ltd. (China) and used without further purification. The chitosan polymerization degrees of 700-1000, 50000, 100000, 150000 and 250000 were adopted in this work. Typically, chitosan (2.0 g, 150000 Mw), $SnCl_4 \cdot 5H_2O$ (0.22 g) and $Ni(NO_3)_2 \cdot 6H_2O$ (3.68 g) were dissolved in 100 mL of 1.25 wt% acetic acid solution at 90 °C and were stirring constantly to generate a mixed homogeneous gel. The acetic acid was adopted to depolymerize the chitosan. The gel was removed water at 50 °C until dried. The dried solid was placed into furnace and calcined in N_2 flow at different calcination temperature ranged from 300 °C to 700 °C for 2 h. The product catalysts were marked as Sn-Ni/CS-X-T, where X represents the molar ratio of metal to chitosan carbon (6/1, 2/1, 1/1, 2/3 and 1/2 were adopted in this work), T represents the calcination temperature (300, 400, 500, 600 and 700 °C were adopted in this work). The typical Ni/Sn molar ratio were fixed to the optimal 20/1 according to our previous works [33], and the additional

Ni/Sn molar ratio of 3/1 was also adopted to compare the effect of Ni_3Sn alloy phase. For comparison, the Ni/CS catalysts and Sn/CS catalysts were synthesized using the same method except without adding $SnCl_4 \cdot 5H_2O$ or $Ni(NO_3)_2 \cdot 6H_2O$. The Sn-Ni/CS (Ni/Sn=3/1) catalyst was synthesized using the same method except with different Ni/Sn molar ratio.

2.2. Catalyst characterization and DFT calculation details

The scanning electron microscope (SEM) and transmission electron microscopy (TEM) were used to observe the textural properties and morphologies of catalysts. The Brunauer-Emmett-Teller (BET) method and Barrett-Joyner-Halanda (BJH) method were carried out to calculate the specific surface area and distribution of pore size, respectively. X-ray diffraction (XRD) analysis was measured the bulk phase and surface state of catalysts. X-ray photoelectron spectroscopy (XPS) was used to analyze the chemical composition of the samples. Temperature programmed desorption of ethanol or acetaldehyde (C_2H_5OH-TPD-MS or C_2H_4O-TPD-MS) and temperature programmed desorption of H_2 (H_2-TPD-MS) experiments were carried out to analyze the desorption of ethanol, acetaldehyde and H_2 over catalysts. The reduction behaviors of the samples were analyzed using temperature programmed reduction (TPR-MS). The metal loadings were determined by inductively coupled plasma optical emission spectroscopy (ICP-OES). More details of catalyst characterization were given in the Supporting Information.

The density functional theory with the PBE form of generalized gradient approximation functional (GGA) [34] was used to calculate the dehydrogenation and the C-C bond breaking processes of C_2H_5OH over pure Ni and Sn-Ni using the Vienna ab-initio simulation package (VASP) [35,36]. More calculation details were described in the Supporting Information.

2.3. Catalytic coupling of aqueous ethanol

The coupling of aqueous ethanol was carried out in a 70 mL autoclave reactor (SSC70 *4-Y2W6–316-GY, Jiangsu Safety Instrument Co., Ltd, Nanjing, China) under magnetic stirring. In a typical experiment run, aqueous ethanol with concentration of 50 wt% and certain amounts of NaOH as well as catalysts were injected to the reactor. Then, the reactor was flushed with H_2 and sealed with H_2 at ambient pressure. Finally, the temperature was raised to 230 °C and kept 12 h. After reaction, the reactor was naturally cooled to room temperature. Both gas and liquid products were collected to further analyze.

2.4. Product analysis

The drainage method was used to measure the gas products, and gas chromatography (GC) was carried out to analyze gas compositions. The liquid sample was centrifuged and the aqueous as well as organic phase products were further analyzed using GC to determine the components and contents. According to the ethanol conversion, C4 + alcohols yield, and product selectivity, the catalytic activity of catalysts was evaluated. More details of instrument parameters and product analysis methods were given in the Supporting Information.

3. Results and discussion

3.1. Characterization of catalysts

3.1.1. The effect of Sn doping on physicochemical property of Ni/CS catalyst

The TEM images of the Ni/CS and Sn-Ni/CS catalysts were shown in Fig. 1a-g. The metal particles were well distributed on the carbon support (Fig. 1a, d) and identified as metal Ni by EDS. The Ni nano particles (NPs) mainly exposed (111) on both Ni/CS and Sn-Ni/CS catalysts, and the (002) facet of Ni_3Sn NPs could also be observed on the Sn-Ni/CS
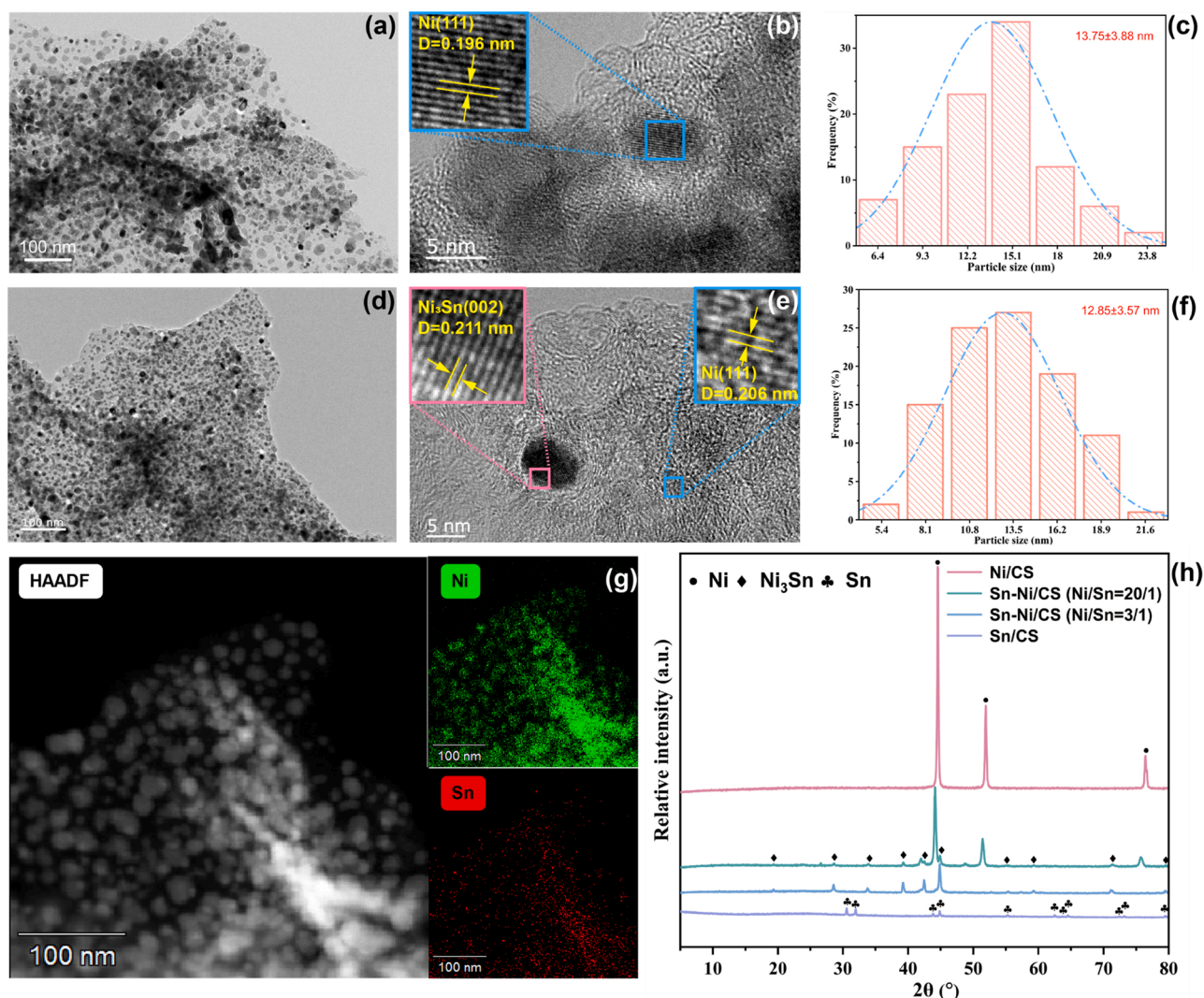
Fig. 1. TEM images (a-b) and statistical size distribution of metal particles (c) of Ni/CS-1/1–500 catalyst. TEM images (d, e and g), statistical size distribution of metal particles (f) and EDS elemental mappings (h-i) of Sn-Ni/CS-1/1–500 catalyst. XRD patterns (h) of Ni/CS catalyst, Sn-Ni/CS (Ni/Sn=20/1) catalyst , Sn-Ni/CS (Ni/Sn=3/1) catalyst and Sn/CS catalyst.

catalyst (Fig. 1b, e). Meanwhile, the lattice spacing of Ni (111) facet (0.206 nm) on Sn-Ni/CS catalysts were observed, which is slightly expanded than that of Ni (111) facet (0.196 nm) on Ni/CS catalysts. The EDS element mapping suggested that Sn were evenly distributed in Ni particles (Fig. 1g). The particle size distribution of Ni/CS and Sn-Ni/CS catalysts were calculated as displayed in Fig. 1c, f, respectively. Compared to the Sn-Ni/CS catalyst (12.85 ± 3.57 nm), the Ni/CS catalyst showed metal particle sizes of 13.75 ± 3.88 nm, which indicated that the Sn doping slightly inhibited the growth of Ni grain.

The XRD was conducted to analysis the bulk phase and surface state of catalysts as shown in Fig. 1h. The detectable peaks of metal Sn or its oxides were not observed in the XRD pattern of Sn-Ni/CS catalysts, indicating the alloying of Ni and Sn. Besides, the diffraction peaks of Ni were mildly shifted to lower 2θ degree with the introduction of Sn in the Sn-Ni/CS catalysts in contrast to Ni/CS catalyst, which could be attributed to the expanded Ni lattice through Sn atoms adding to the face-centered cubic (fcc) structure of Ni [37–39]. According to the PDF (04–0850 and 35–1362) of XRD, the Ni₃Sn diffraction peaks were detected in Sn-Ni/CS (Ni/Sn=3/1) catalyst, but the Ni diffraction peaks were barely observed, which was due to the formation of Ni₃Sn alloy at Ni/Sn molar ratio of 3/1. This result is in accord with the TEM analysis.

The XPS was carried out to examine the surface electronic states and

chemical composition of the catalysts. Fig. 2 showed XPS spectra of the Ni/CS and Sn-Ni/CS catalysts. The adjusted C-C bond binding energy was 284.8 eV. The peaks located at 286.3, 288.9 and 531.5 eV were assigned to the C-O, O-C=O and C=O bonds (Fig. 2a, c) [40,41]. Fig. 2b showed the peaks at 403.2, 400.4 and 398.7 eV were correspond to the pyridine oxide-N, graphitic-N and pyridinic-N bonds [42]. These bonds above should be assigned to the chitosan precursor. As displayed in Fig. 2d, the peaks of Ni⁰ and Ni²⁺ species were mainly determined in Ni 2p₃/₂ bond peaks of Sn-Ni/CS. Significantly, an additional peak of NiO (metallic oxide) was found in the Ni 2p₃/₂ bond peaks of Ni/CS compared to Sn-Ni/CS. The O 1s spectra of Ni/CS also showed additional MOₓ (metallic oxide) bonding peak compared to Sn-Ni/CS. These results indicated more NiO metallic oxide without Sn doping, which was further verified by the strong reduction peak of Ni/CS in H₂-TPR-MS (Fig. S1). These results indicated the reduction of Ni²⁺ species was promoted effectively with the Sn doping. It is worth noting that with Sn doping, the binding energy of Ni⁰ shifts to lower energy at a rate of 0.2 eV (Fig. 2e), which should be caused by the charge transfer from the Sn to Ni. For the Sn 3d spectra (Fig. 2f), the surface state of Sn with metallic and oxidic was showed, but discrimination between Sn (II) and Sn (IV) species was difficult due to the negligible binding energy of those species.
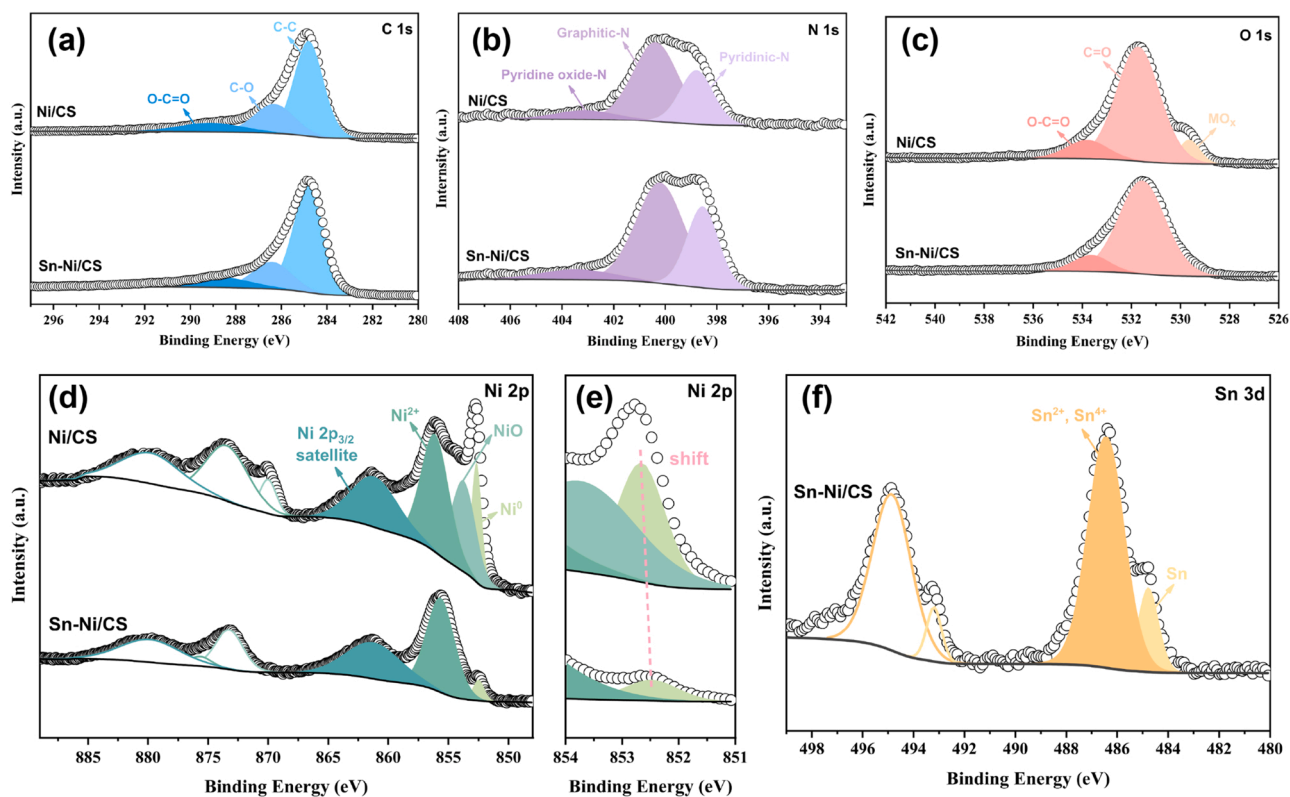
Fig. 2. XPS spectra of the Ni/CS-1/1–500 catalysts and Sn-Ni/CS-1/1–500 catalysts: (a) C 1s spectra, (b) O 1s spectra, (c) N 1s spectra, (d, e) Ni 2p spectra and (f) Sn 3d spectra.
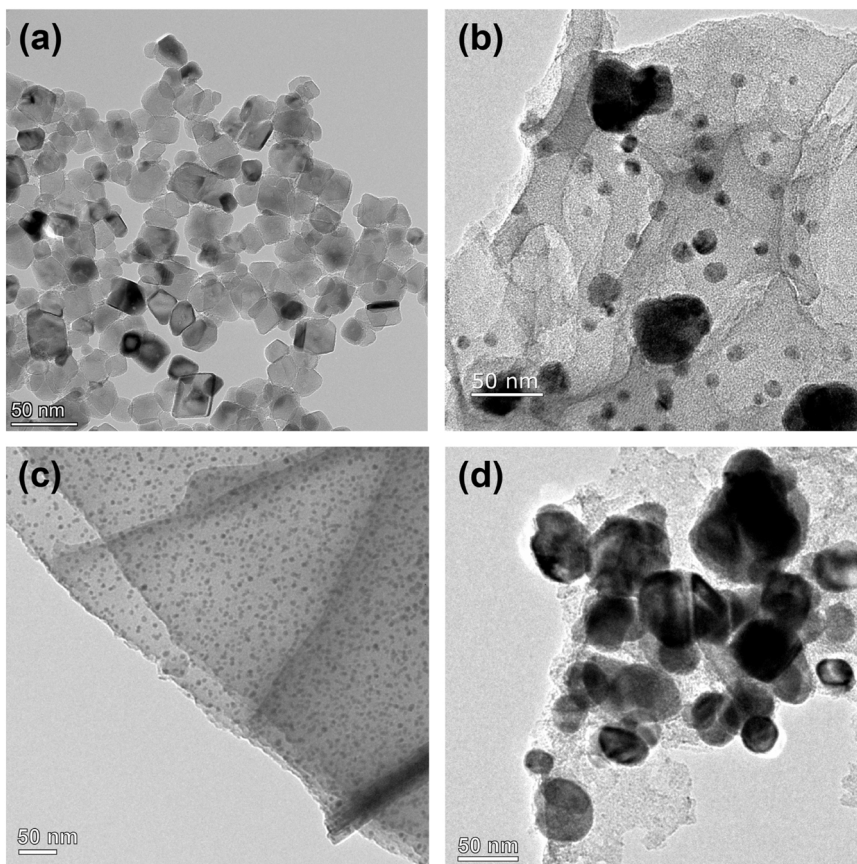

Fig. 3. TEM images of Sn-Ni/CS-X-T catalyst: (a) Sn-Ni/CS-6/1–500, (b) Sn-Ni/CS-1/2–500, (c) Sn-Ni/CS-1/1–300 catalyst, (d) Sn-Ni/CS-1/1–700 catalyst.

3.1.2. The effect of preparation conditions on physicochemical property of Sn-Ni/CS catalysts

The morphology and microstructure of the catalysts were analyzed through TEM (Fig. 3). Clearly, the metal nanoparticles were embedded in carbon layers (Fig. S2). Furthermore, the TEM image of Sn-Ni/CS-6/1–500 catalyst showed only metal nanoparticles, without obvious carbon layers (Fig. 3a). The Sn-Ni/CS-1/2–500 samples showed abundant carbon layers (Fig. 3b). The catalysts treated with carbonization temperature of 300 °C showed abundant carbon layers and small particle size of metal nanoparticles (Fig. 3c). The carbon layers tended to be porous with the increase of carbonization temperature, which would be beneficial for increasing the surface area of catalyst (Fig. S2b, c). Nevertheless, metal agglomeration and growth would be occurred with the increase of carbonization temperature (Fig. 3d). Taken together, the suitable M/CS ratio and carbonization temperature are crucial to obtain well reduced and dispersed metallic Ni active center as well as large specific surface area.

The nitrogen porosimetry test results of the synthesized Sn-Ni/CS-1/1-T samples were shown in Table 1 and Fig. S3. Generally, all of the prepared Sn-Ni/CS catalysts exhibited typical IV type isotherm, hysteretic rings in high range of P/P$_0$ (Fig. S3b) and average pore diameter (Table 1), which indicated the mesoporous structure. With raising the carbonization temperature, the BET surface area of Sn-Ni/CS-T catalyst gradually increased, reached the maximum of 54.0 m^2/g at 500 °C and then decreased (Table 1). The surface area decreased at high calcination temperature because the chitosan decomposed and carbonized severely as well as the metal particles aggregated. The elemental content of Sn-Ni/CS-1/1-T samples was determined by ICP-OES analysis (Table 1). The molar ratio of Ni/Sn was varied in the range of 18.8–23.6, which closed to 20/1. The metal content increased with the calcination temperature raised.

The crystal phase of prepared Sn-Ni/CS-X-500 samples were determined using XRD (Fig. 4a). The peaks for NiO, Ni and Ni$_3$Sn were occurred in XRD patterns of the prepared Sn-Ni/CS-6/1–500 and Sn-Ni/CS-2/1–500 catalysts, while other catalysts didn't show distinct NiO diffraction peaks. This should be attributed to the insufficient proportion of carbon precursor with metal/CS ratio of 6/1 and 2/1, resulting in partial reduction of NiO. Furthermore, the intensity of Ni$_3$Sn and Ni diffraction peaks obviously decreased with the M/CS ratio decreased from 1/1 to 1/2, which should be caused by the formation of thick carbon layers and small particle size of metal nanoparticles. The XPS spectra was shown in Fig. 4b-c and Fig. S4a-c. For metal/CS ratio of 6/1 and 2/1, the intensity of the high valence and oxidation states for Ni and Sn increased as shown in Ni 2p, Sn 3d spectra (Fig. 4b, c), and the O 1s spectra (Fig. S4c) also showed the MO$_x$ bonding peak decreased with metal/CS ratio decreased, which was consistent with the prior XRD analysis (Fig. 4a). Moreover, the binding energy of Ni^0 shifted to lower energies with metal/CS ratio increased, corresponding to the binding energy of Sn^{2+}, Sn^{4+} shifted to higher energies [37].

The crystal phase of prepared Sn-Ni/C-1/1-T catalysts were also identified by XRD as displayed in Fig. 4d. With carbonization temperature raising, the intensity of Ni peaks obviously enhanced, and the characteristic diffraction peak of Ni$_3$Sn gradually appeared and showed a trend of enhancement. Notably, the NiO cannot be entirely reduced with carbonization temperature of 300 °C, thus the NiO crystal phase still existed. Nevertheless, severe metal gain agglomeration occurred as the carbonization temperature as high as 700 °C, which was consisting with the TEM analysis. The XPS spectra was shown in Fig. 4e-f and Fig. S4d-f, and the metal chemical state compositions were determined based on Ni 2p$_{3/2}$ and Sn 3d$_{5/2}$ peaks as displayed in Table S2. For Ni 2p, Sn 3d and O 1s spectra (Fig. 4e-f and Fig. S4f), the NiO and MO$_x$ peaks were only observed on Sn-Ni/CS-1/1–300 catalyst, and the proportion of metallic state Ni^0 and Sn^0 increased with carbonization temperature increased (Table S2), which was consisting with the prior XRD results (Fig. 4d). Moreover, the binding energy of Ni^0 shifted to lower energies at the low carbonization temperature such as 300–400 °C, which could be related to the enhanced electron transfer from Sn to Ni [37].

3.1.3. The texture stability of optimal Sn-Ni/CS catalysts

The TEM was used to analyze the morphology of the spent catalysts (Fig. 5a-c). The catalyst maintains a good structure of dispersed nanoparticle after 12 h reaction (0th recycle, Fig. 5a), which is the same as the fresh catalyst as presented in Fig. 1d. Besides, the XRD patterns of the 0th recycle Sn-Ni/CS-1/1–500 catalysts also showed negligible difference with the fresh catalyst (Fig. 5d). Nevertheless, some vacancies on the catalyst were observed after 5th cycle runs, and the catalyst kept well structure stability after further 10th cycle runs (Fig. 5c). The XRD patterns also showed the intensity of Ni diffraction peaks obviously decreased after 5 cycle runs. The ICP-OES result of the 10th recycle Sn-Ni/CS-1/1–500 catalyst showed the metal content of 78.7 wt%, which decreased slightly compared to the fresh catalyst (82.5 wt%) indicating that part of unconfined metal particles was leached during the hydrothermal reaction process. These results indicated that only little part of unconfined Ni particles was leaching after 5th hydrothermal reactions, and then the catalyst kept stable even after 10th cycle runs.

3.2. Catalytic coupling of aqueous ethanol over Sn-Ni/CS

Herein, for Sn-Ni/CS catalyst, the effect of M/CS ratio (X) on the upgrading performance was firstly investigated. Table 2 shows the overall performance of ethanol aqueous upgrading over Sn-Ni/CS-X-500 catalysts. For chitosan carbon, it's inactive for the ethanol coupling process (Table S3), it mainly played the role of dispersing and protecting active metal nanoparticles. The Sn-Ni/CS-1/1–500 catalyst exhibited excellent performance with 60.9% ethanol conversion and 37.3% C4 + higher alcohols yield. The produced higher alcohols mainly include straight chain alcohols and isomeric alcohols with 2-ethyl group, such as n-butanol, 2-ethyl butanol, etc., and C10 + alcohols are almost isomeric alcohols. Compared with commonly reported typical catalysts for ethanol upgrading (Table S1), the non-noble Sn-Ni/CS-1/1–500 catalyst exhibited excellent ethanol conversion and higher alcohols yield. With the M/CS ratio aggrandized from 1/1 to 6/1, ethanol conversion obviously decreased from 60.9% to 6.7% caused by the insufficient reduction of Ni on the sample with high M/CS ratio (Fig. 4a). Nevertheless, the Sn-Ni/CS-1/2–500 catalyst with low M/CS ratio also exhibited poor catalytic activity, which might be caused by mass transfer resistance from the excess thick carbon shell. It's worth noting that Sn-Ni/CS-2/3–500 catalyst gave a similar ethanol conversion and higher alcohol yield to Sn-Ni/CS-1/1–500 catalyst, but the Sn-Ni/CS-2/3–500 catalyst exhibited poor carbon chain growth capacity of 0.339 (Table 2). Thus, the Sn-Ni/CS catalysts with M/CS ratio of 1/1 showed the best performance for aqueous ethanol coupling.

The carbonization temperature is also crucial for the chemical state of catalyst and its catalytic activity. Fig. 6a, b shows the overall catalytic activities of ethanol aqueous upgrading over Sn-Ni/CS-1/1-T catalysts, in which the catalytic performances are correlated closely with the
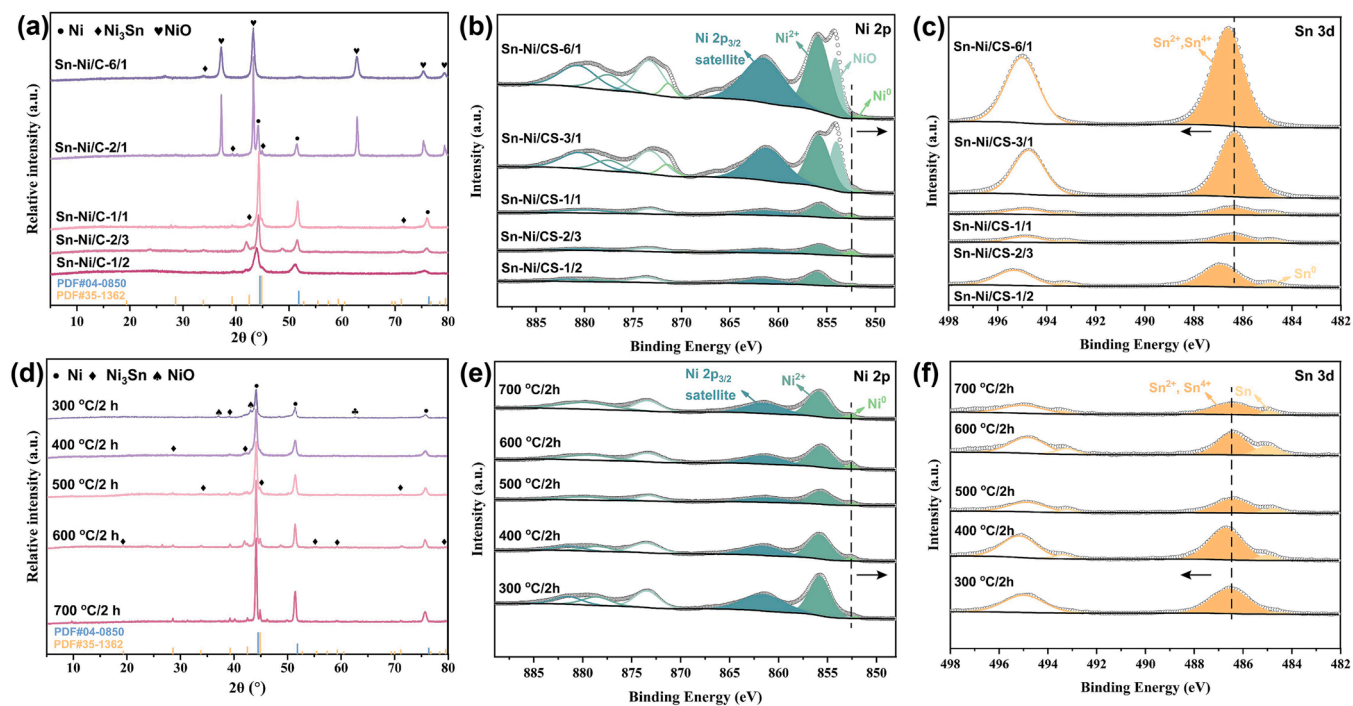
Table 1
Texture properties of the Sn-Ni/CS catalysts.

Catalyst[a]	S$_{BET}$ (m^2/g)	Pore Volume (cm^3/g)	Average Pore D^a (nm)	Molar ratio of Ni/Sn	Metal[b] (wt%)
Sn-Ni/CS-300	30	0.05	8.7	21.9	82.2
Sn-Ni/CS-400	33	0.03	7.9	23.6	82.3
Sn-Ni/CS-500	54	0.05	8.2	22.2	82.5
Sn-Ni/CS-600	36	0.04	6.8	18.8	83.9
Sn-Ni/CS-700	33	0.03	5.5	22.7	83.5

[a] : The Ni/Sn and M/CS ratio of all catalysts were 20/1 and 1/1, respectively.
[b] : Metal included Ni and Sn.

Fig. 4. XRD patterns and XPS spectra of Sn-Ni/CS-X-500 catalysts synthesized under different M/CS: (a) XRD patterns, (b) Ni 2p spectra, (c) Sn 3d spectra; XRD patterns and XPS spectra of Sn-Ni/CS-1/1-T catalysts synthesized under different carbonization temperature: (d) XRD patterns, (e) Ni 2p spectra, (f) Sn 3d spectra. (The Ni/Sn ratio of all catalysts were 20/1.).
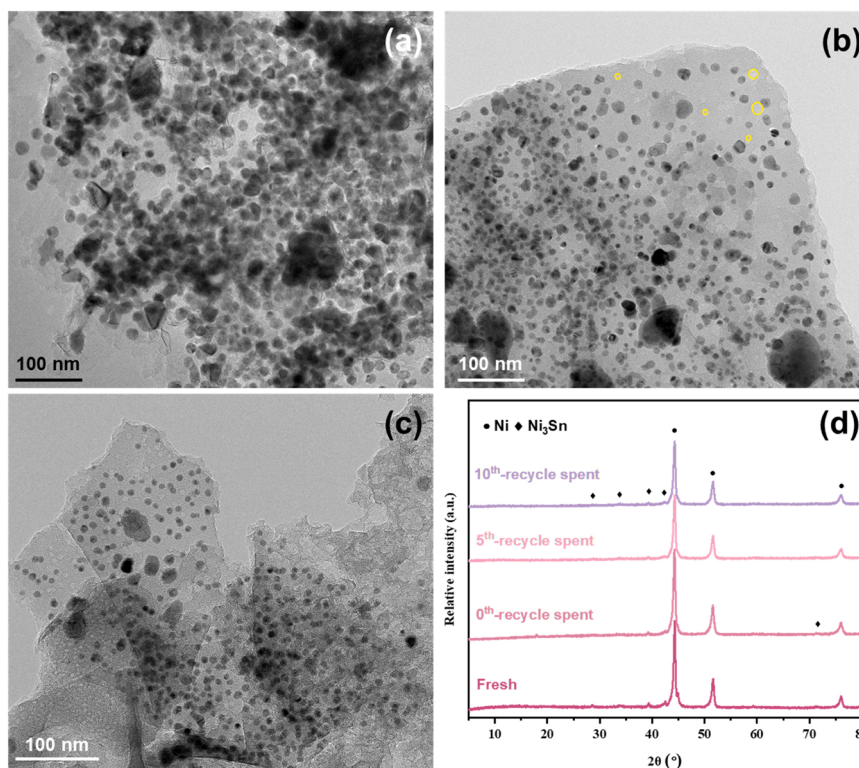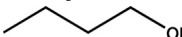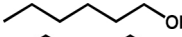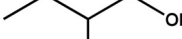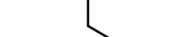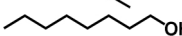

Fig. 5. TEM images (a-c) and XRD patterns (d) of the fresh and recycled Sn-Ni/CS-1/1–500 catalyst: (a) 0th recycled, (b) 5th recycled, (c) 10th recycled.

catalyst carbonization temperature (a volcano type curve). With the raise of carbonization temperature, the ethanol conversion as well as higher alcohols yield gradually increased and reached the highest at carbonization temperature of 500 °C, then the activity of the catalyst declined as the carbonization temperature further increased.

Particularly, the Sn-Ni/CS-1/1–700 catalyst exhibited quite poor activity with ethanol conversion of only 15.1%, which could be due to the severe metal grain agglomeration occurred at high carbonization temperature of 700 °C as the prior XRD and TEM revealed (Fig. 4d and Fig. 3d). It is worth noting that Sn-Ni/CS-1/1 catalysts carbonized at

Table 2
Overall catalytic activities of ethanol aqueous upgrading over Sn-Ni/CS-X-500 catalysts.

Catalyst	Sn-Ni/CS				
M/CS, molar ratio	6/1	2/1	1/1	2/3	1/2
EtOH Conv., C%	6.7	9.6	60.9	65.5	18.8
Yield of higher alcohol, C%	2.4	2.2	37.3	33.4	5.8
Carbon balance, C%	97.3	99.2	86.0	80.2	93.9
Step-growth probability α[a]	0.136	0.189	0.378	0.339	0.169
Alcohol product selectivity, C%					
(n-alcohol) OH	42.5	46.1	42.0	42.8	71.2
(alcohol) OH	4.2	6.0	15.8	16.1	4.8
(iso-alcohol) OH	5.7	8.2	11.5	11.7	5.3
(n-alcohol) OH	–	–	5.3	5.4	–
(iso-alcohol) OH	–	–	5.5	5.6	–
C10 + n-alcohol	–	–	1.6	1.7	–
C10 + iso-alcohol	–	–	4.7	4.8	–

Reaction conditions: 0.3 g Sn-Ni/C-X-500 catalysts, 0.87 g NaOH, 10 g EtOH, 10 g H_2O ; 230 °C, 12 h.

[a] : The α represented step-growth probability, which was calculated according to the reported step-growth polymerization model [26,43].

400–600 °C showed similar catalytic performances, while the Sn-Ni/CS-1/1–500 catalyst showed superior carbon chain growth capacity (Fig. 6b). Therefore, the carbonization temperature of 500 °C was optimized.

Since chitosan is a macromolecular polymer, the effect of chitosan polymerization degree on the coupling performance was investigated. As presented in Fig. 6c, overall, the Sn-Ni/CS-1/1–500 catalysts with different molecular weight of chitosan exhibited comparable catalytic activity, and the Sn-Ni/CS-1/1–500 catalyst derived from chitosan of 150000 Mw exhibited the highest higher alcohols yield of 37.3%. It could be due to that the chitosan was depolymerized in an aqueous solution with appropriate concentration of acetic acid and the depolymerization did not change other structure just randomly along the backbone [44]. In the same dissolution time and temperature, molecular weight of chitosan decreased to 1000-30000 Mw [31,45], and this is why only catalyst with 700–1000 Mw molecular weight of chitosan had a little lower catalytic activity than other catalysts.

The reusability of Sn-Ni/CS-1/1–500 catalyst for ethanol coupling to C4 + alcohols in the aqueous system were researched. After each reaction finished, the recycled catalyst was washed using deionized water, which was carried out to catalyze the next recycle reaction under the same conditions mentioned above. As presented in Fig. 6d, the recycled Sn-Ni/CS-1/1–500 clearly exhibited excellent catalytic stability with ethanol conversion decline less than 2% in 10th recycle runs. Significantly, the slightly decreased catalytic performance after 5th cycle could be related to the loss of unconfined metal particles from carbon carrier
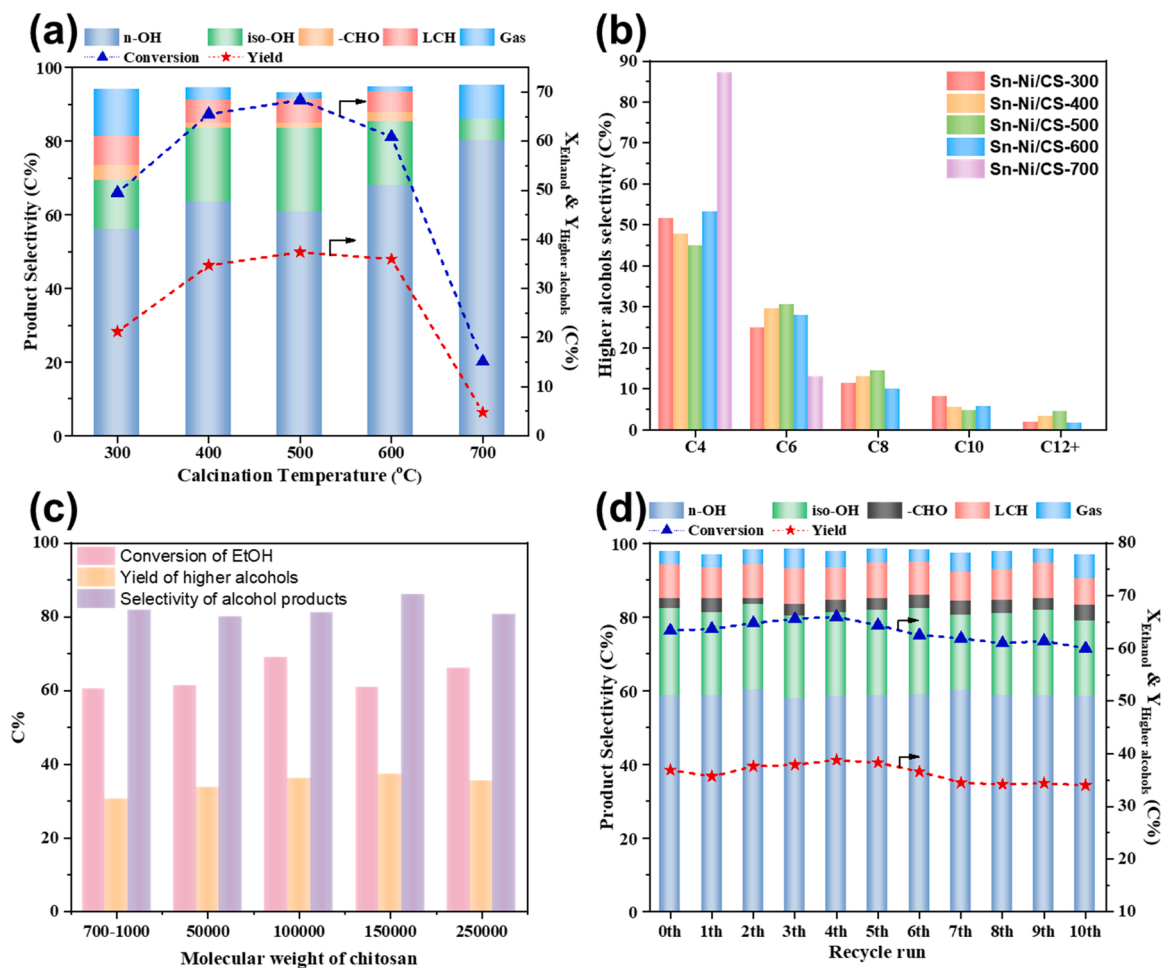

Fig. 6. Overall catalytic performance of ethanol aqueous coupling over Sn-Ni/CS catalysts: (a-b) Sn-Ni/CS-1/1-T catalysts, (c) Sn-Ni/CS-1/1–500 catalysts with different molecular weight of chitosan, (d) recycled Sn-Ni/CS-1/1–500 catalysts. (Reaction conditions: 0.3 g catalysts, 0.87 g NaOH, 10 g EtOH, 10 g H_2O; 230 °C, 12 h. Others: unidentified species.).

during the aqueous reaction and the centrifugal washing process (Fig. 5).

3.3. Catalytic mechanism of Sn doping

The beneficial effect of Sn doping had been found in our previous research [26,33], but the promoting mechanism still need to be further studied. Here, a series of experiments were carried out to study the promoting mechanism of Sn doping on catalytic performance and the active phase of Sn-Ni/CS catalyst. The Ni/CS and Sn/CS catalysts prepared with the same fabrication process were employed separately to examine their catalytic performance for aqueous ethanol upgrading as shown in Table 3. Obviously, the Sn-Ni/CS catalyst exhibited superior catalytic performance comparing with Ni/CS and Sn/CS catalysts, which gave the 60.9% ethanol conversion and 37.3% higher alcohols yield. Nevertheless, the Ni/CS catalyst only gave 32.1% conversion and 5.9% higher alcohols yield, and the selectivity of undesired gas by-products reached up to 14.1%, which is about 10 times of that over Sn-Ni/CS catalyst. Meanwhile, the very poor activity of Sn/CS catalyst suggests the Sn is inactive for the activation of ethanol molecular. The physical mixed Ni/CS and Sn/CS catalyst also exhibited poor catalytic performance comparing to individual Ni/CS catalyst, which should be attributed to the lessened Ni active component. Therefore, these results implied the catalytic performance can be promoted only by doping of Sn to Ni as the bimetallic catalyst rather than physical mixing. Besides, it is remarkable that the Sn-Ni/CS catalyst with Ni/Sn ratio of 3/1 also showed poor catalytic performance, in which the Ni_3Sn alloy component dominated the catalyst (XRD pattern in Fig. 1h). Combined with the above results, it indicated the main active phase of Sn-Ni/CS catalyst was still Ni, and the introduced Sn probably worked through modifying the electron property of Ni active sites.

Generally, the aqueous ethanol upgrading involves multi-step hydrogen transfer and aldol condensation reactions. The metal sites play a crucial part in the hydrogen transfer reaction, while the aldol condensation process is carried out on the base sites [15]. As showed in Table S3, the reaction without base also demonstrated the crucial role of NaOH for aldol condensation, and the further consumption of aldehyde intermediates could lead to equilibrium shift of alcohol dehydrogenation. To further verify the effect of Sn doping on dehydrogenation and hydrogenation process, the online sampling ethanol dehydrogenation and acetaldehyde hydrogenation reactions over Ni/CS and Sn-Ni/CS catalysts were performed, respectively. The concentration trend of acetaldehyde and C4 + higher alcohol products during ethanol dehydrogenation over Ni/CS and Sn-Ni/CS catalysts were shown in Fig. 7a, b. For Sn-Ni/CS catalyst, it's clear that the concentration of acetaldehyde showed a volcano type curve and the concentration of C4 + alcohols increased gradually within 12 h. Whereas, the concentration of C4 + higher alcohols over Ni/CS catalyst increased quickly within 2 h and reached stability during the next 10 h reaction time. These results implied the formation of acetaldehyde was enhanced over Sn-Ni/CS, which could further promote the aldol condensation process to obtain higher alcohols. For the acetaldehyde hydrogenation over Ni/CS and Sn-Ni/CS samples, the concentration of acetaldehyde and hydrogenation product within 12 h reaction time were shown in Fig. 7c, d. Clearly, the acetaldehyde was gradually consumed, and the ethanol formed by direct hydrogenation of acetaldehyde increased gradually. Obviously, the hydrogenation activity of Ni/CS is higher than that of Sn-Ni/CS. The TPD of H_2 was further conducted to illustrate the effect of Sn doping on the H_2 absorption behavior (Fig. S5). It was noticeable that the H_2 desorption peaks shifted forward and desorption intensity reduced on Sn-Ni/CS sample compared to that of Ni/CS, which verified the doping of Sn weakened H_2 adsorption and inhibited the acetaldehyde hydrogenation reaction. In short, the doping of Sn to Ni catalyst enhanced the formation of acetaldehyde and weakened the hydrogenation activity.

The characterization results showed that the doping of Sn had a vital effect on the structure of the Ni-based catalysts, and the changes of structure led to the difference of catalytic performance over the Ni/CS and Sn-Ni/CS catalysts. The C_2H_5OH-TPD-MS was carried out to investigate the adsorption properties of ethanol and the selectivity of products respectively over Ni/CS and Sn-Ni/CS catalysts. The C_2H_5OH-TPD profiles of Ni/CS catalyst and Sn-Ni/CS catalyst were shown in Fig. 8a, b. The peaks at $m/z = 2, 16, 28$ and 46 were correspond to the molecular ion of H_2, CH_4, CO and C_2H_5OH, respectively. As shown in Fig. 8c, the peaks at 111 °C for Ni/CS and 100 °C for Sn-Ni/CS can be attributed to weak adsorption of ethanol. However, the peak of the Sn-Ni/CS appeared at a lower temperature than that of Ni/CS, which indicated ethanol was more easily desorbed from Sn-Ni/CS than that Ni/CS. The TPD pattern of CO resulted from ethanol reforming (Fig. 8d) showed the CO peaks over Ni/CS appeared at higher temperature than that over Sn-Ni/CS. The TPD pattern of CH_4 (Fig. 8e) showed ethanol was cleaved into CH_4 at 232 °C and 307 °C over Ni/CS catalyst. However, the first peak of CH_4 appeared at 296 °C over Sn-Ni/CS catalyst, which could be attributed to the fact that Sn doping inhibited the cleaving of C-O and C-C bond of ethanol.

The adsorption of intermediates imposes crucial effect on the dehydrogenation reaction pathway and product selectivity. The C_2H_4O-TPD-MS was adopted to investigate the adsorption properties of acetaldehyde on Ni/CS and Sn-Ni/CS catalysts, respectively. The curve of mass $m/z = 29$ was detected, which signified the desorption of acetaldehyde. As presented in Fig. 8f, the desorption peaks at 92 °C and 104 °C over Ni/CS and Sn-Ni/CS catalysts corresponded to weak adsorption of acetaldehyde. The peaks at 253 °C for Ni/CS and 146 °C for Sn-Ni/CS were related to the desorption of acetaldehyde on the metal sites. The acetaldehyde desorption temperature of Ni/CS was higher than that of Sn-Ni/CS, which indicated that the interaction between acetaldehyde and the metal sites of Sn-Ni/CS was weakened after Sn doped. It can be caused by the electron repulsion effect between the electron-rich O atom of CH_3CHO and the electron-rich Ni sites of the Sn-Ni/CS [46]. The weakened adsorption of aldehyde intermediate over Sn-Ni/CS effectively suppressed deep dehydrogenation and cleaving of acetaldehyde, and the desorbed aldehydes then proceeded the aldol-type C-C coupling to generate higher alcohols over aqueous alkali center.

Table 3
Comparison of catalytic performance for ethanol aqueous upgrading over various catalysts.

Cat.	EtOH Conv.%	Yield (Selectivity)						Carbon balance
		n-OH	iso-OH	-CHO	LCH	Gas[a]	Others[b]	
Sn-Ni/CS (Ni/Sn=20/1)	60.9	29.0 (68.3)	8.3 (18.1)	1.0 (2.7)	2.4 (5.2)	0.5 (1.3)	2.2 (4.4)	86.0
Ni/CS	53.9	20.6 (57.5)	5.1 (14.3)	0.5 (1.3)	2.8 (7.8)	5.1 (14.1)	1.8 (5.0)	87.0
Sn/CS	6.8	1.7 (81.5)	0.3 (15.7)	0.0 (0.0)	0.0 (0.0)	0.0 (0.0)	0.1 (2.8)	95.2
Sn-Ni/CS (Ni/Sn=3/1)	22.1	8.4 (57.8)	0.7 (5.1)	0.8 (5.6)	1.5 (10.2)	1.6 (10.1)	1.5 (10.1)	97.4
Ni/CS, Sn/CS[c]	47.09	17.56 (50.5)	3.0 (11.3)	0.5 (3.3)	1.8 (9.9)	4.5 (17.8)	1.2 (7.2)	86.5

Reaction conditions: 0.3 g catalysts, 0.87 g NaOH, 10 g EtOH, 10 g H_2O; 230 °C, 12 h.
[a] : Gas product included H_2, CO, CO_2 and C1-C6 hydrocarbons.
[b] : Others were unidentified species.
[c] : Ni/CS catalyst and Sn/CS catalyst were physically blended and (Ni/CS)/(Sn/CS) = 20/1.
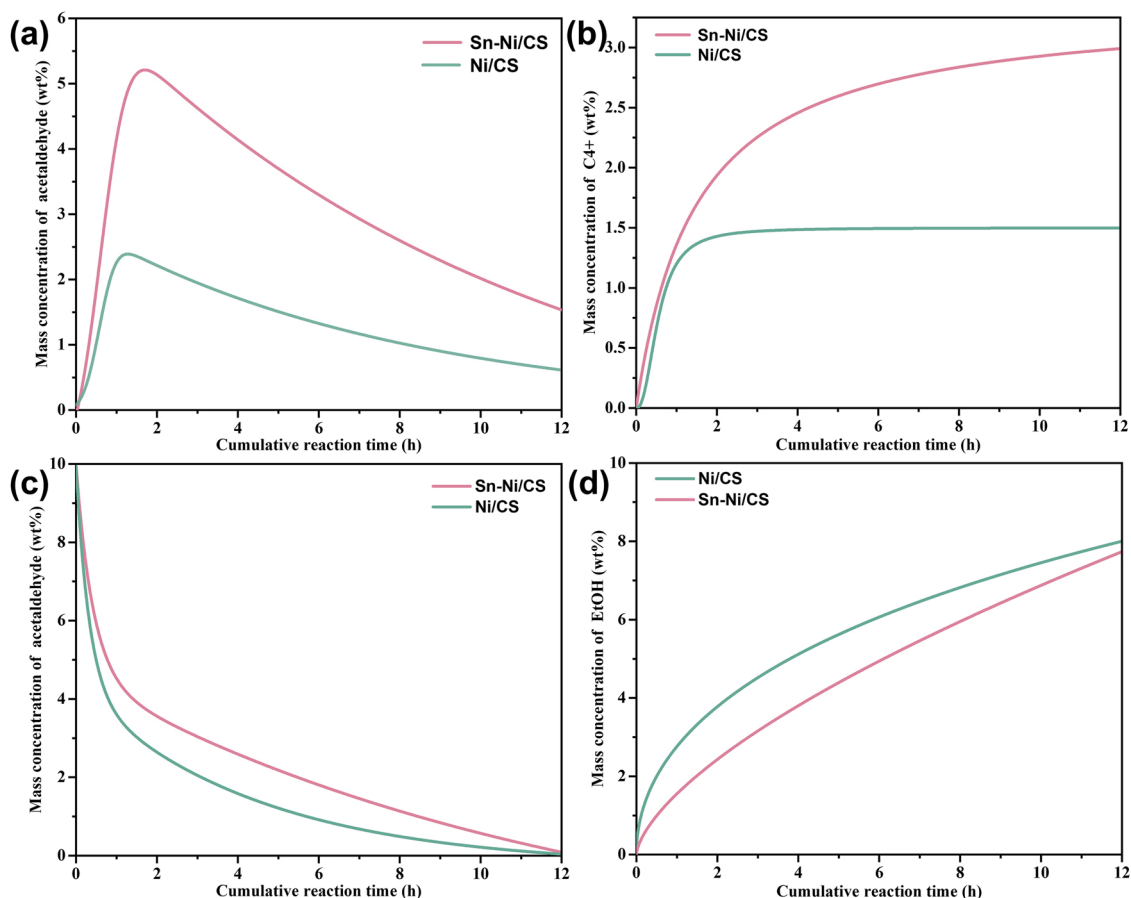
Fig. 7. Online sampling reaction over Ni/CS and Sn-Ni/CS catalysts: (a-b) Online sampling in ethanol dehydrogenation process (0.36 g catalysts, 12 g EtOH, 12 g H₂O; 230 °C, 0.1 MPa, 12 h), (c-d) Online sampling in acetaldehyde hydrogenation process (0.36 g catalysts, 2.4 g acetaldehyde, 21.6 g H₂O; 40 °C, 5.0 MPa, 12 h).

To further investigate the influence of doped Sn on molecular level, the density functional theory study was employed to illustrate mechanism for ethanol dissociation on Sn-Ni and Ni, respectively. Based on prior experiment results, the Ni should be the main active sites, and Sn is less active because the Sn-4d orbital is fully occurred. Thus, the Ni atom was defined as active center in our calculation. As shown in Fig. 9, four main steps in the dissociation of ethanol are involved. The first step is dehydrogenation ($CH_3CH_2OH^* \rightarrow CH_3CH_2O^* + H^*$, Fig. S6a), the similar energy barriers on both sites are observed (Fig. 9a), indicating that the doped Sn has little influence on such process. However, the Sn-Ni shows lower activity than Ni for the second dehydrogenation step. To proceed the reaction, the CH_3CHO^* adsorption structure will be transferred to more stable $CH_3CHO(d)^*$ double-site adsorption structures (Fig. S7). Such processes are exothermic for both Ni and Sn-Ni, while the former one shows more energy reduced (blue line in Fig. 9a). For $CH_3CHO(d)^* \rightarrow CH_3CO^* + H^*$ (Fig. 9b), the energy barrier on Ni is lower by 0.15 eV than that of Sn-Ni, indicating that the doped Sn will hinder the further dehydrogenation of CH_3CHO, which is favorable for the stable existence of CH_3CHO substrate. Finally, for the C-C dissociation step (Fig. 9a, c), it can be noted that the energy barrier on Ni is lower than Sn-Ni, indicating the C-C dissociation is not favorable on Sn-Ni. This is well consistent with the experiment results that the C-C dissociation was suppressed on Sn-Ni.

Take into consideration the TPD-MS and DFT results, it's rational to infer that the weakened adsorption of aldehyde intermediate over Sn-doped Ni contributed to the enhanced formation of aldehyde and suppressed breaking of C-C bond. And the adsorption behavior of catalyst should be tightly connected with surface electronic structure change by doping Sn as prior XPS observed, thus the charge density distribution of the active sites was further simulated. As shown in Fig. 9d, the doped Sn significantly changed the surface charge distribution of Ni sites, and more electrons accumulated around Ni atoms. In addition, the activated Ni atom in Sn-Ni was employed by the d-band-center theory of Norskov et al.[47]. For partial density of state (Fig. 9e, f), it can be seen that the d-band-center of active Ni atom on Sn-Ni (−1.30 eV) is lower than that of pure Ni (−1.21 eV), which indicated that electrons were concentrated on Ni and this is agreement with the XPS results. As a result, the electronegative Sn-doped Ni sites showed electron repulsion effect to the electron-rich O atom in aldehyde, thus weakened the adsorption of aldehyde intermediate.

3.4. Proposed plausible mechanism for aqueous ethanol coupling over Sn-Ni/CS catalyst

According to the above characterization and experiments results, it's reasonable to propose the reaction pathway as showed in Fig. 10. Ethanol is firstly adsorbed on the Ni sites, and then dehydrogenate to acetaldehyde. With Sn doped, the electron transfers from Sn to Ni forming the electron-rich Ni sites, which bring the electron repulsion effect to the electron-rich O atom of CH_3CHO. Thus, the adsorption of aldehyde intermediate is weakened and the further breaking of C-C bond is suppressed, which facilitates the desorption of aldehyde intermediates from Ni sites and promotes aldol condensation C-C coupling over aqueous $[OH]^-$ alkali center. Finally, the butyraldehyde intermediates are hydrogenated to form butanol, and the as-formed higher alcohols proceed the step-growth process continuously to form C4 + higher alcohols.
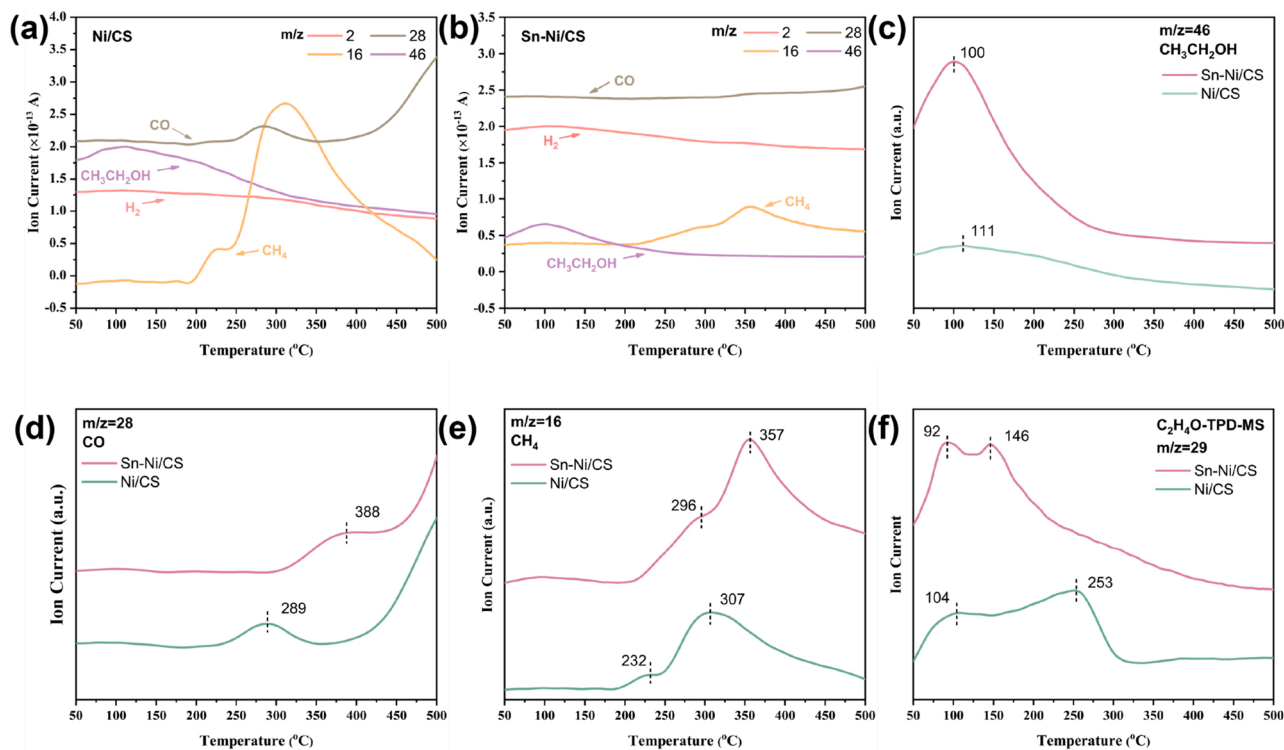
Fig. 8. (a) TPD profiles over Ni/CS catalyst, (b) TPD profiles over Sn-Ni/CS catalyst, (c) C$_2$H$_5$OH-TPD profiles of C$_2$H$_5$OH, (d) C$_2$H$_5$OH-TPD profiles of CO, (e) C$_2$H$_5$OH -TPD profiles of CH$_4$, (f) C$_2$H$_4$O-TPD profiles.
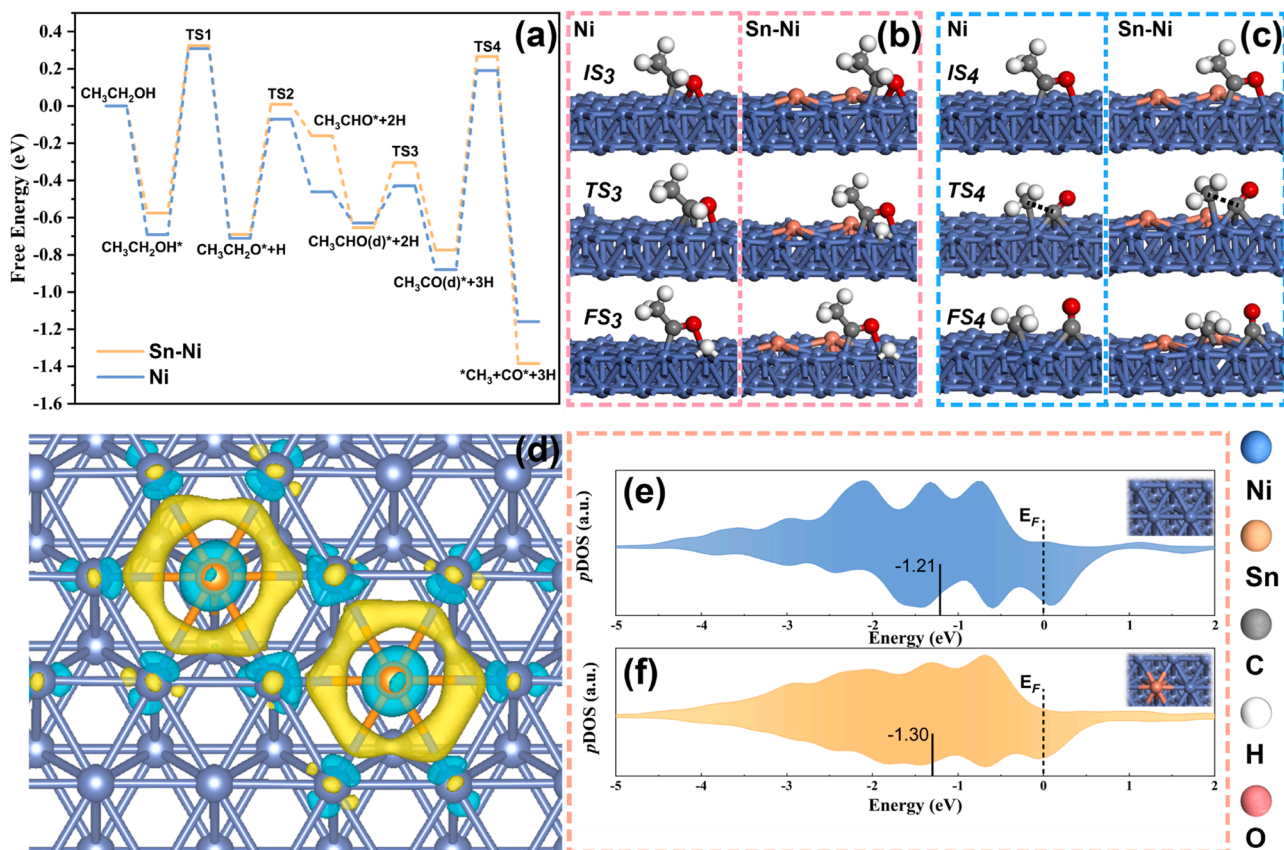

Fig. 9. (a) Free energy diagrams in ethanol dissociation over Ni and Sn-Ni, (b, c) Configuration diagrams of initial state (IS), transition state (TS) and final state (FS) for the dehydrogenation and C-C cleavage of ethanol on the Ni (111) and Sn-Ni (111) models, (d) The differential charge for Sn-Ni (the yellow and blue area denote the electron accumulation and lost), (e, f) The d-band-center of active Ni atom on Ni (e) and Sn-Ni (f).
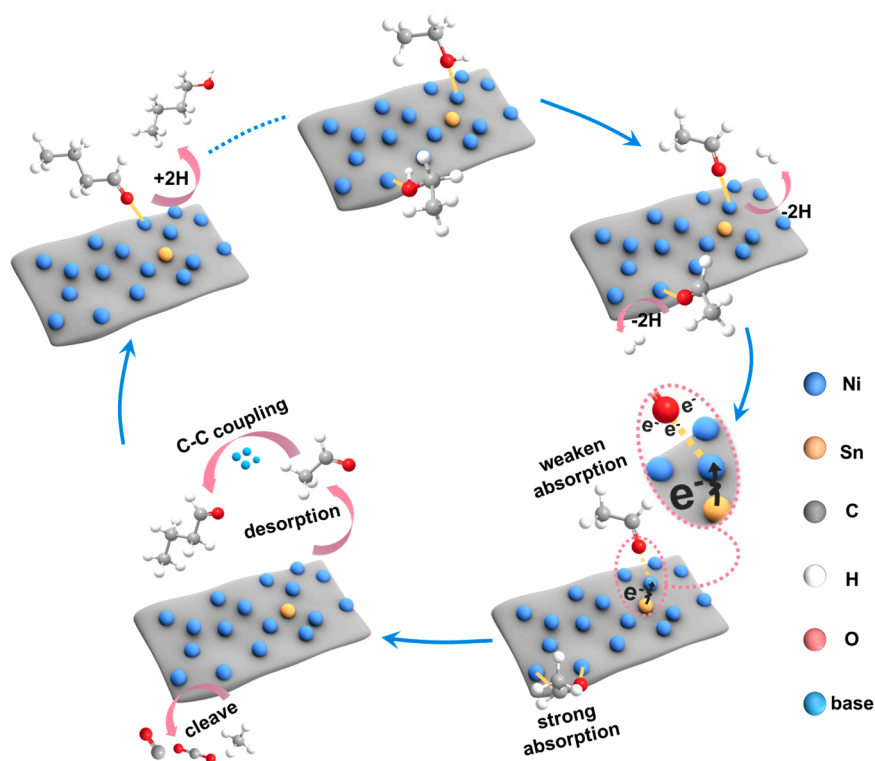
Fig. 10. The proposed plausible mechanism for ethanol coupling to higher alcohol over Sn-Ni/CS catalysts.

4. Conclusion

In this work, the chitosan derived Sn-Ni/CS nanocomposites were fabricated and achieved excellent catalytic performance in the direct aqueous ethanol coupling of to higher alcohols. The optimized Sn-Ni/CS catalyst exhibited excellent activity and reusability with 60% ethanol conversion and 86.4% higher alcohol selectivity. The doping of Sn clearly boosted the C-C coupling process and suppressed the C-C cleavage side reaction. The beneficial effect of Sn was demonstrated to be closely associated with the weakened adsorption of aldehyde intermediates, which should be caused by the electron repulsion effect between aldehyde and the electronegative Sn-doped Ni sites. Thus, the desorption of aldehyde intermediates from Ni sites is facilitated over Sn-Ni/CS catalyst, those aldehydes then further proceed the aldol-type C-C coupling process over aqueous alkali center instead of breaking C-C bond on Ni sites.

Author Contributions

Conceptualization: T. Wang, Q. Zhang and S. Qiu; Methodology: B. Chen, Q. Zhang and H. Dong; Validation: B. Chen and X. Zheng; Formal analysis: Q. Zhang, B. Chen and H. Dong; Investigation: B. Chen, Q. Zhang and J. Gu; Resources: T. Wang, Q. Zhang; Data curation: B. Chen and X. Zheng; Writing – original draft: B. Chen and Q. Zhang; Writing – review & editing: T. Wang, S. Qiu and J. Song; Visualization: Q. Zhang, X. Wu and S. Qiu; Supervision: T. Wang; Project administration: T. Wang; Funding acquisition: T. Wang and Q. Zhang. All authors have read and agreed to the published version of the manuscript.

CRediT authorship contribution statement

Bo Chen: Writing – original draft, Methodology, Validation, Investigation, Formal analysis, Data curation, Software. **Xinqi Zheng**: Methodology, Validation, Investigation, Data curation. **Juwen Gu**: Investigation. **Songbai Qiu**: Conceptualization, Writing – review & editing, Visualization. **Jinliang Song**: Writing – review & editing. **Xiaoping Wu**: Visualization. **Huafeng Dong**: Methodology, Formal analysis. **Qian Zhang**: Conceptualization, Formal analysis, Resources, Methodology, Writing – original draft, Visualization, Funding acquisition. **Tiejun Wang**: Conceptualization, Writing – review & editing, Supervision, Funding acquisition, Resources, Project administration.

Declaration of Competing Interest

The authors declare that they have no known competing financial interests or personal relationships that could have appeared to influence the work reported in this paper.

Data availability

Data will be made available on request.

Acknowledgments

Appendix A. Supporting information

Supplementary data associated with this article can be found in the online version at doi:10.1016/j.apcatb.2022.122048.

References

[1] J.T. Kozlowski, R.J. Davis, Heterogeneous catalysts for the guerbet coupling of alcohols, ACS Catal. 3 (2013) 1588–1600.

[2] Y. Wang, J. Liu, Z. Zhao, Q. Guo, Q. Jiang, N. He, F. Wang, A carbon-negative route for sustainable production of aromatics from biomass-derived aqueous oxygenates, Appl. Catal. B Environ. 307 (2022), 121139.

[3] H. Wang, Q. Wang, Y. Tong, Y. Wu, J. Peng, X.-K. Gu, M. Ding, Selective C-O bond activation of biomass-derived γ-valerolactone to biofuels over MFI-mediated co-based synergetic catalysts, Appl. Catal. B Environ. (2022), 121840.

[4] M.J. Climent, A. Corma, S. Iborra, Conversion of biomass platform molecules into fuel additives and liquid hydrocarbon fuels, Green Chem. 16 (2014) 516–547.

[5] H. Hosseinzadeh-Bandbafha, M. Tabatabaei, M. Aghbashlo, M. Khanali, A. Demirbas, A comprehensive review on the environmental impacts of diesel/biodiesel additives, Energy Convers. Manag. 174 (2018) 579–614.

[6] A.C. Hansen, Q. Zhang, P.W.L. Lyne, Ethanol–diesel fuel blends — a review, Bioresour. Technol. 96 (2005) 277–285.

[7] A.I. Lampe, A.K. Dittmar, C. Heyen, J. Kiefer, Butanol as a potential biofuel: a spectroscopic study of its blends with n-decane and diesel, Fuel 222 (2018) 312–318.

[8] P. Dürre, Biobutanol: an attractive biofuel, Biotechnol. J. 2 (2007) 1525–1534.

[9] Q. Zhong, J. Liao, Q. Zhang, S. Qiu, Q. Meng, X. Wu, T. Wang, Aqueous upgrading of ethanol to higher alcohol diesel blending and jet fuel precursors over Na-doped porous Ni@C nanocomposite, Fuel 324 (2022).

[10] M. Wang, R. Dewil, K. Maniatis, J. Wheeldon, T. Tan, J. Baeyens, Y. Fang, Biomass-derived aviation fuels: challenges and perspective, Prog. Energy Combust. Sci. 74 (2019) 31–49.

[11] B. Yuan, J. Zhang, Z. An, Y. Zhu, X. Shu, H. Song, X. Xiang, W. Wang, Y. Jing, L. Zheng, J. He, Atomic Ru catalysis for ethanol coupling to C4+ alcohols, A Appl. Catal. B Environ. 309 (2022).

[12] M. Xue, B. Yang, C. Xia, G. Zhu, Upgrading ethanol to higher alcohols via biomass-derived Ni/Bio-apatite, ACS Sustain. Chem. Eng. 10 (2022) 3466–3476.

[13] B. Bharathiraja, J. Jayamuthunagai, T. Sudharsanaa, A. Bharghavi, R. Praveenkumar, M. Chakravarthy, D. Yuvaraj, Biobutanol – an impending biofuel for future: a review on upstream and downstream processing tecniques, Renew. Sustain. Energy Rev. 68 (2017) 788–807.

[14] A. Gupta, J.P. Verma, Sustainable bio-ethanol production from agro-residues: a review, Renew. Sustain. Energy Rev. 41 (2015) 550–567.

[15] J. Pang, M. Zheng, Z. Wang, S. Liu, X. Li, X. Li, J. Wang, T. Zhang, Catalytic upgrading of ethanol to butanol over a binary catalytic system of FeNiOx and LiOH, Chin. J. Catal. 41 (2020) 672–678.

[16] N.V. Kulkarni, W.W. Brennessel, W.D. Jones, Catalytic upgrading of ethanol to n-butanol via manganese-mediated guerbet reaction, ACS Catal. 8 (2018) 997–1002.

[17] X. Fei, Q. Xu, L. Xue, X. Zhong, Z. Zhang, K. Liu, X. Lin, T. Wang, Y. Qin, X. Qiu, Aqueous phase catalytic conversion of ethanol to higher alcohols over NiSn bimetallic catalysts encapsulated in nitrogen-doped biorefinery lignin-based carbon, Ind. Eng. Chem. Res. 60 (2021) 17959–17969.

[18] Y. Wang, M. Peng, J. Zhang, Z. Zhang, J. An, S. Du, H. An, F. Fan, X. Liu, P. Zhai, D. Ma, F. Wang, Selective production of phase-separable product from a mixture of biomass-derived aqueous oxygenates, Nat. Commun. 9 (2018) 5183.

[19] R.L. Wingad, P.J. Gates, S.T.G. Street, D.F. Wass, Catalytic conversion of ethanol to n-butanol using ruthenium P–N ligand complexes, ACS Catal. 5 (2015) 5822–5826.

[20] S. Chakraborty, P.E. Piszel, C.E. Hayes, R.T. Baker, W.D. Jones, Highly selective formation of n-butanol from ethanol through the guerbet process: a tandem catalytic approach, J. Am. Chem. Soc. 137 (2015) 14264–14267.

[21] M. Leon, E. Diaz, S. Ordonez, Ethanol catalytic condensation over Mg-Al mixed oxides derived from hydrotalcites, Catal. Today 164 (2011) 436–442.

[22] Q.-N. Wang, B.-C. Zhou, X.-F. Weng, S.-P. Lv, F. Schueth, A.-H. Lu, Hydroxyapatite nanowires rich in [Ca-O-P] sites for ethanol direct coupling showing high C6-12 alcohol yield, Chem. Commun. 55 (2019) 10420–10423.

[23] Q. Zhang, J. Dong, Y. Liu, Y. Wang, Y. Cao, Towards a green bulk-scale biobutanol from bioethanol upgrading, J. Energy Chem. 25 (2016) 907–910.

[24] G. Wang, S. Zhang, X. Zhu, C. Li, H. Shan, Dehydrogenation versus hydrogenolysis in the reaction of light alkanes over Ni-based catalysts, J. Ind. Eng. Chem. 86 (2020) 1–12.

[25] M. Khorasani-Motlagh, M. Noroozifar, M.-S. Ekrami-Kakhki, Investigation of the nanometals (Ni and Sn) in platinum binary and ternary electrocatalysts for methanol electrooxidation, Int. J. Hydrog. Energy 36 (2011) 11554–11563.

[26] W. Liu, B. Chen, Q. Zhang, S. Qiu, X. Wu, Q. Meng, L. Ma, T. Wang, One-pot synthesis of high-carbon bio-alcohols from aqueous ethanol upgrading over water-tolerance NiSn@C catalyst, Energy Convers. Manag. 249 (2021), 114822.

[27] X. Wu, X. Cai, Q. Zhang, P. Bi, Q. Meng, Y. Pi, T. Wang, Upgrading of aqueous bioethanol to higher alcohols over NiSn/MgAlO catalyst, ACS Sustain. Chem. Eng. 9 (2021) 11269–11279.

[28] Q. Liu, H. Wang, H. Xin, C. Wang, L. Yan, Y. Wang, Q. Zhang, X. Zhang, Y. Xu, G. W. Huber, L. Ma, Selective cellulose hydrogenolysis to ethanol using Ni@C combined with phosphoric acid catalysts, ChemSusChem 12 (2019) 3977–3987.

[29] L. Lang, Y. Shi, J. Wang, F.-B. Wang, X.-H. Xia, Hollow core–shell structured Ni–Sn@C nanoparticles: a novel electrocatalyst for the hydrogen evolution reaction, ACS Appl. Mater. Interfaces 7 (2015) 9098–9102.

[30] C. Gerente, V.K.C. Lee, P. Le Cloirec, G. McKay, Application of chitosan for the removal of metals from wastewaters by adsorption - mechanisms and models review, Crit. Rev. Environ. Sci. Technol. 37 (2007) 41–127.

[31] C.T. Tsao, C.H. Chang, Y.Y. Lin, M.F. Wu, J.L. Han, K.H. Hsieh, Kinetic study of acid depolymerization of chitosan and effects of low molecular weight chitosan on erythrocyte rouleaux formation, Carbohydr. Res. 346 (2011) 94–102.

[32] Y. Pi, X. Wu, Z. Zheng, L. Ma, T. Wang, Chitosan-lignin carbon framework-encapsulated Cu catalyst facilitates base-free hydrogen evolution from methanol/water, Catal. Sci. Technol. 12 (2022) 1941–1949.

[33] Q. Zhang, W. Liu, B. Chen, S. Qiu, T. Wang, Upgrading of aqueous ethanol to fuel grade higher alcohols over dandelion-like Ni-Sn catalyst, Energy Convers. Manag. 216 (2020).

[34] J.P. Perdew, K. Burke, M. Ernzerhof, Generalized gradient approximation made simple, Phys. Rev. Lett. 77 (1996) 3865–3868.

[35] G. Kresse, J. Furthmüller, Efficiency of ab-initio total energy calculations for metals and semiconductors using a plane-wave basis set, Comput. Mater. Sci. 6 (1996) 15–50.

[36] G. Kresse, J. Furthmüller, Efficient iterative schemes for ab initio total-energy calculations using a plane-wave basis set, Phys. Rev. B 54 (1996) 11169–11186.

[37] J.H. Kim, S.M. Choi, S.H. Nam, M.H. Seo, S.H. Choi, W.B. Kim, Influence of Sn content on PtSn/C catalysts for electrooxidation of C1–C3 alcohols: synthesis, characterization, and electrocatalytic activity, Appl. Catal. B Environ. 82 (2008) 89–102.

[38] L.R. Vidales-Gallardo, E.N. Armendáriz-Mireles, G.G. Suarez-Velázquez, E. Rocha-Rangel, W.J. Pech-Rodríguez, Green and cost-effective synthesis of NiSn alloys by using intermittent microwave heating process as electrocatalysts for ethanol oxidation in alkaline solution, J. Mater. Res. (2021).

[39] Y. Ma, J. Liu, M. Chen, Q. Yang, H. Chen, G. Guan, Y. Qin, T. Wang, Selective hydrogenation of naphthalene to decalin over surface-engineered alpha-MoC based on synergy between Pd doping and Mo vacancy generation, Adv. Funct. Mater.

[40] Y. Shao, C. Cao, S. Chen, M. He, J. Fang, J. Chen, X. Li, D. Li, Investigation of nitrogen doped and carbon species decorated TiO$_2$ with enhanced visible light photocatalytic activity by using chitosan, Appl. Catal. B Environ. 179 (2015) 344–351.

[41] Y. Li, J. Ma, D. Jin, G. Jiao, X. Yang, K. Liu, J. Zhou, R. Sun, Copper oxide functionalized chitosan hybrid hydrogels for highly efficient photocatalytic-reforming of biomass-based monosaccharides to lactic acid, Appl. Catal. B Environ. 291 (2021), 120123.

[42] X. Yu, R. Nie, H. Zhang, X. Lu, D. Zhou, Q. Xia, Ordered mesoporous N-doped carbon supported Ru for selective adsorption and hydrogenation of quinoline, Microporous Mesoporous Mater. 256 (2018) 10–17.

[43] P.A. Cuello-Penaloza, R.G. Dastidar, S.-C. Wang, Y. Du, M.P. Lanci, B. Wooler, C. E. Kliewer, I. Hermans, J.A. Dumesic, G.W. Huber, Ethanol to distillate-range molecules using Cu/MgxAlOy catalysts with low Cu loadings, Appl. Catal. B Environ. 304 (2022).

[44] D. Kuehbeck, G. Saidulu, K.R. Reddy, D. Diaz Diaz, Critical assessment of the efficiency of chitosan biohydrogel beads as recyclable and heterogeneous organocatalyst for C-C bond formation, Green Chem. 14 (2012) 378–392.

[45] A. Pandit, L. Khare, P. Ganatra, R. Jain, P. Dandekar, Intriguing role of novel ionic liquids in stochastic degradation of chitosan, Carbohydr. Polym. 260 (2021), 117828.

[46] Y. Wang, L. Shi, W. Lu, Q. Sun, Z. Wang, C. Zhi, A.-H. Lu, Spherical boron nitride supported gold-copper catalysts for the low-temperature selective oxidation of ethanol, Chemcatchem 9 (2017) 1363–1367.

[47] J.K. Nørskov, Electronic factors in catalysis, Prog. Surf. Sci. 38 (1991) 103–144.